

Cite this: *Integr. Biol.*, 2014, 6, 53

Enhanced luminescence of $\text{CaMoO}_4\text{:Eu}$ by core@shell formation and its hyperthermia study after hybrid formation with Fe_3O_4 : cytotoxicity assessment on human liver cancer cells and mesenchymal stem cells†

A. K. Parchur,^a A. A. Ansari,^b B. P. Singh,^c T. N. Hasan,^d N. A. Syed,^d S. B. Rai^a and R. S. Ningthoujam^{*e}

Highly water dispersible Eu^{3+} doped CaMoO_4 nanoparticles (core) covered by CaMoO_4 (shell) have been prepared using the polyol method. Significant enhancement in luminescence intensity by core@shell formation is observed due to the decrease of non-radiative rate arising from surface/defect of particles. Effect of 266 nm laser excitation (Mo–O charge transfer band) on the asymmetric ratio (A_{21} = intensity ratio of electric to magnetic dipole transitions) has been studied and compared with a xenon lamp source. Luminescence intensity increases with the increase of power at 532 nm laser excitation. In order to explore materials, which can show dual functionalities such as luminescence as well as magnetic properties (magnetization of $\sim 14.2 \text{ emu g}^{-1}$), water dispersible $\text{Fe}_3\text{O}_4\text{--CaMoO}_4\text{:Eu}$ hybrid magnetic nanoparticles (MN) have been prepared. This shows good heating ability up to $\sim 42^\circ\text{C}$ (hyperthermia) and luminescence in the red region ($\sim 612 \text{ nm}$), which is in a biological window (optical imaging). Biocompatibility of the synthesized $\text{Fe}_3\text{O}_4\text{--CaMoO}_4\text{:Eu}$ hybrid magnetic nanoparticles has been evaluated *in vitro* by assessing their cytotoxicity on human liver cancer cells (HepG2 cells) and hTERT cells using the MTT assay and fluorescent microscopy studies.

Received 15th July 2013,
Accepted 19th October 2013

DOI: 10.1039/c3ib40148k

www.rsc.org/ibiology

Insight, innovation, integration

Highly water dispersible Eu^{3+} doped CaMoO_4 (core) covered by inactive CaMoO_4 (shell) nanoparticles have been successively prepared using the polyol method. Significant enhancement in luminescence intensity by core@shell formation was observed. $\text{Fe}_3\text{O}_4\text{--CaMoO}_4\text{:Eu}$ hybrid magnetic nanoparticles show both luminescence and magnetic behavior (saturation of magnetization $\sim 14.2 \text{ emu g}^{-1}$). Furthermore, hybrid magnetic nanoparticles show good heating ability up to $\sim 42^\circ\text{C}$ (hyperthermia) and luminescence in the red region ($\sim 612 \text{ nm}$), which is in a biological window (optical imaging). Biocompatibility of the hybrid magnetic nanoparticles has been evaluated *in vitro* by assessing their cytotoxicity on human liver cancer cells (HepG2 cells) and hTERT cells.

1. Introduction

In recent years, there has been enormous interest in the synthesis of rare-earth ion (Ln^{3+}) doped core and core@shell

nanoparticles due to their wide applications.^{1–18} These materials can be extensively used in optoelectronic and biological applications. Moreover, core@shell and/or hybrid nanomaterials having both magnetic and luminescence properties are used in magnetic resonance imaging (MRI), *in vitro* and *in vivo* bio-labelling, drug delivery and hyperthermia applications.^{19–21} In general, Fe_3O_4 magnetic nanoparticles (MN) are used in hyperthermia applications by coating the surface of nanoparticles using different surfactants, like, oleic acid (OA), dimercaptosuccinic acid (DMSA), chitosan (CS), *O*-carboxymethyl chitosan (OCMCS) and poly-ethylene glycol (PEG), *etc.*^{20,22–24} However, it is difficult to prepare material, which can show luminescence as well as magnetic properties. Generally, luminescence intensity decreases with an increase of ferromagnetic species in the material.¹ For this, it is

^a Department of Physics, Banaras Hindu University, Varanasi-221005, India

^b King Abdullah Institute for Nanotechnology, King Saud University, Riyadh-11451, Saudi Arabia

^c Department of Physics, Indian Institute of Technology (BHU), Varanasi-221005, India

^d Research & Development, Bharathiar University, Coimbatore-641046, India

^e Chemistry Division, Bhabha Atomic Research Centre, Mumbai-400085, India.
E-mail: nraghu_mani@yahoo.co.in, rsn@barc.gov.in; Fax: +91-22-25505151;
Tel: +91-22-2559321

† Electronic supplementary information (ESI) available. See DOI: 10.1039/c3ib40148k

necessary to optimize the concentration of magnetic and luminescence materials to be used. Common techniques are (i) formation of the shell of Ln^{3+} doped inorganic host on a surface modified Fe_3O_4 nanoparticles (core@shell structures), (ii) mixing of proper amounts of Fe_3O_4 nanoparticles with inorganic phosphor nanomaterials (hybrid structures) and (iii) a MN-inert shell/organic ligand–phosphor system (*e.g.*, liposome/vesicle in which MN is in the core (water dispersible) and phosphor is in the lipid layer (oil dispersible). Recently, some nanocomposites such as $\text{Fe}_3\text{O}_4@\text{Y}_2\text{O}_3:\text{Eu}^{3+}$,²⁵ $\text{Fe}_3\text{O}_4@\text{YVO}_4:\text{Eu}^{3+}$,²⁶ $\text{Fe}_3\text{O}_4@\text{YPO}_4:\text{Eu}/\text{Tb}^{3+}$,²⁷ *etc.* were prepared and their luminescence, magnetic and induction heating properties were studied. The methods used for the preparation of such nanoparticles needed a long time, and particles were inhomogeneous in shape. Usually, Fe_3O_4 magnetic nanoparticles were prepared by a co-precipitation method, and these were used for a hyperthermia application due to their high biocompatibility.²³ In particular, nanoparticles with surface functionalization are more useful in biological applications.^{28–30} Gd based nanoparticles are used for cancer therapy through hyperthermia as well as a contrast agent in MRI.³¹

In most cases, $\text{CaMoO}_4:\text{Eu}$ particles are not dispersible in a polar medium. This makes them less suitable for biological and polymer based display applications. In order to make them dispersible, there are a few ways: (i) particle size should be <50 nm and (ii) surface functionalization. Enhanced luminescence intensity for dispersed particles is important, and thus it can be achieved by use of a functionalized ligand having a lower number of O–H and C–H and core@shell formations. Luminescence intensity is also dependent on the type of solvent where nanoparticles are dispersed, excitation wavelength and power density. These are not discussed much in the literature. In this paper, significant enhancement in luminescence of Eu^{3+} doped CaMoO_4 nanoparticles (core) is achieved by forming inactive CaMoO_4 (shell) on the surface of the core. The power density dependent luminescence using a 532 nm Nd:YAG laser is studied so that the desired luminescence intensity can be obtained. $\text{Fe}_3\text{O}_4@\text{CaMoO}_4:\text{Eu}$ hybrid nanoparticles are prepared for hyperthermia applications. To the best of our knowledge, for the first time these hybrid nanoparticles with excellent dispersibility, heating ability up to $\sim 42^\circ\text{C}$ and luminescence properties have been prepared. Bio-compatibility of hybrid nanoparticles on cancerous and normal cells was studied.

2. Experimental section

2.1 Preparation

2.1.1 Preparation of $\text{CaMoO}_4:\text{Eu}@\text{CaMoO}_4$ nanoparticles. $\text{CaMoO}_4:\text{Eu}^{3+}$ ($\text{Eu}^{3+} = 1, 3, 5, 7, 10, 15, 20$ and 30 at%) were prepared at a low-temperature $\sim 150^\circ\text{C}$ using urea hydrolysis in ethylene glycol (EG) as a medium as well as a capping agent. The detailed preparation of $\text{CaMoO}_4:\text{Eu}^{3+}$ is described elsewhere.⁴ The as-prepared samples were divided into three parts: the second and third parts were annealed at 500 and 900°C for 4 h each to grow the crystallite size and to remove the unwanted dangling bonds on the surface of the nanoparticles. The as-prepared sample was considered as a core.

In a typical process for the synthesis of core@shell nanoparticles ($\text{CaMoO}_4:\text{Eu}@\text{CaMoO}_4$ with stoichiometry of $1:1$ mole ratio), core nanoparticles obtained by the above are added to 50 mL of EG and 2 g of urea followed by ultrasonication for 30 min. To this, a stoichiometric amount of Ca^{2+} and MoO_4^{2-} ions dispersed in a minimum amount of distilled water are added to the above solution under continuous stirring and is allowed to heat the solution at 120 – 150°C for 2 h. The precipitate so obtained was centrifuged and excess of EG was removed by adding methanol and acetone. The particles obtained were allowed to dry at room temperature for ~ 48 h.

2.1.2 Preparation of Fe_3O_4 magnetic nanoparticles. The superparamagnetic Fe_3O_4 nanoparticles ($\text{Fe}_3\text{O}_4\text{-MN}$) were prepared using the co-precipitation method discussed earlier.²² $\text{Fe}_3\text{O}_4\text{-MN}$ nanoparticles were prepared by ferric chloride ($\text{FeCl}_3\cdot 6\text{H}_2\text{O}$) and ferrous sulphate ($\text{FeSO}_4\cdot 7\text{H}_2\text{O}$) in a NH_3 medium. In order to prepare dispersible particles in water, 4 g of PEG was dissolved in 50 mL of distilled water and treated with the $\text{Fe}_3\text{O}_4\text{-MN}$. It was kept for ultrasonication for 30 min to get homogeneous mixing.

2.1.3 Preparation of hybrid MN ($\text{Fe}_3\text{O}_4\text{-CaMoO}_4:\text{Eu}$). For the preparation of the $\text{Fe}_3\text{O}_4\text{-CaMoO}_4:\text{Eu}$ hybrid MN ($1:4$ mole ratio), 28.94 mg of Fe_3O_4 and 100 mg $\text{CaMoO}_4:\text{Eu}$ were dispersed in 4 mL of distilled water containing 1 g of polyethylene glycol (PEG) and followed by ultrasonication for 30 min. The resulting hybrid nanoparticles dispersed in PEG were used for hyperthermia experiments. The hybrid nanoparticles were collected after centrifugation and allowed to dry in an ambient atmosphere for 4 days. This powder was used to record luminescence of the sample.

2.1.4 Culture and maintenance of HepG2 and hTERT cell lines. The HepG2 hepatoblastoma cells and hTERT human mesenchymal cells were maintained between 10% and 90% confluency and propagated in 90% Eagle's Minimal Essential Medium (EMEM) (ATCC) and RPMI 1640, respectively. Media were supplemented with 10% fetal bovine serum (FBS) (ATCC) and 1% penicillin/streptomycin ($10\,000$ I.U. mL^{-1} – $10\,000$ $\mu\text{g mL}^{-1}$) (ATCC). Cells were cultured as adherent monolayers (*i.e.*, cultured at $\sim 70\%$ to 80% confluence) and maintained at 37°C in a humidified atmosphere of 5% CO_2 . Cells were harvested after brief trypsinization.

2.1.5 MTT assay. Cytotoxicity was determined by the yellow 3-(4,5-dimethyl thiazol-2-yl)-2,5-diphenyltetrazolium bromide (MTT) assay.³² The MTT assay is based on the ability of viable cells to reduce soluble MTT into an insoluble, blue formazan product. In brief, around 10^5 cells per well were plated in 96-well microtiter plates in a 100 μL of EMEM medium. After 24 h the medium was changed, and cells were treated with $\text{Fe}_3\text{O}_4\text{-CaMoO}_4:\text{Eu}$ hybrid magnetic nanoparticles at different concentrations ($0, 5, 10, 20, 40, 80, 160, 320, 640$ $\mu\text{g mL}^{-1}$) for 24 h. After this, the medium was aspirated off and 100 μL MTT (0.5 mg mL^{-1}) was added and incubated for 4 h. The liquid from each well was aspirated and discarded. The formazan crystals formed during incubation with MTT was solubilised by adding 100 μL of dimethyl sulfoxide (DMSO) to each well. The plates were placed on a shaker for 15 min for complete solubilization of crystals, and the optical density of each well was determined. The quantity of formazan product as measured by

the amount of 545 nm absorbance is directly proportional to the number of living cells in culture. The cell viability (%) related to control wells containing cell culture medium without Fe₃O₄-CaMoO₄:Eu hybrid magnetic nanoparticles as a vehicle was calculated by:

$$\text{Viability (\%)} = [A]_{\text{test}}/[A]_{\text{control}} \times 100 \quad (1)$$

where $[A]_{\text{test}}$ is the absorbance of the test sample and $[A]_{\text{control}}$ is the absorbance of control sample. IC₅₀ was also calculated. Triplicate experiments were carried out.

To examine the morphological changes in the nucleus and the cytoplasm of cells after addition of Fe₃O₄-CaMoO₄:Eu hybrid magnetic nanoparticles into HepG2 cells and hTERT, fluorescent microscopy was performed. The HepG2 and hTERT cells, approximately 1×10^5 , were cultured in 6 well plates in a medium made up of EMEM and treated with IC₅₀ and the highest concentration ($640 \mu\text{g mL}^{-1}$) of Fe₃O₄-CaMoO₄:Eu hybrid magnetic nanoparticles, respectively, for 24 h with technical triplicates. Untreated control and treated cells were observed under an inverted microscope (Carl Zeiss, Deutschland). For each experiment, nuclei from 10 random fields of wells were examined at 200 times magnification. DAPI, a fluorescent dye was used for examining the treatment of HepG2 cells with Fe₃O₄-CaMoO₄:Eu hybrid magnetic nanoparticles.

4'-6-Diamidino-2-phenylindole (DAPI) is known to form fluorescent complexes with natural double-stranded DNA, showing fluorescence specificity for adenine-thymine (AT), and adenine-uracil (AU) clusters. Because of this property, DAPI is a useful tool in various cytochemical investigations. When DAPI binds to DNA, its fluorescence is strongly enhanced. Also, there is also evidence that DAPI binds to the minor groove, stabilized by hydrogen bonds between DAPI and acceptor groups of AT and AU base pairs. The membrane permeable fluorescent dye DAPI ($2 \mu\text{g mL}^{-1}$) (Sigma Aldrich), which binds to the chromatin of cells, was added to the fixed cells.

2.2 Characterization of magnetic and luminescence nanoparticles

X-ray diffraction (XRD) patterns of the powder samples were examined at room temperature using a PANalytical X'Pert X-ray diffractometer equipped with Ni filtered Cu K α ($\lambda = 1.54056 \text{ \AA}$) radiation as the X-ray source. Raman spectra was recorded on a Jobin Yvon Horiba HR800, UV Raman microscope using a HeNe laser emitting at 632.8 nm. Excitation and emission spectra of all the samples were recorded using an Edinburgh Instrument FLS920 having 450 W xenon lamp. The emission spectra were also recorded using 266 nm excitation from a Nd:YAG laser and 532 nm excitation from laser (Verdi V5). A Horiba Jobin Yvon iHR320 spectrometer was used to detect the luminescence signal.

Induction heating of hybrid magnetic nanoparticles was performed in a 1.5 mL micro centrifuge tube, which was placed at the centre of a 6 cm diameter copper coil coated with Teflon[®] (Easy Heat 8310, Ambrell, UK). In a typical measurement, 5 mg of hybrid nanoparticles were dispersed in 1 mL of distilled water, which was inside a 1.5 mL microcentrifuge tube. AC magnetic field at different currents and fixed at 265 kHz was applied.

Heat generated within the sample was recorded using an optical temperature sensor. Temperature was measured with an accuracy of $\pm 0.01 \text{ }^\circ\text{C}$. The resultant magnetic field at the centre of the 6 cm copper coil was calculated using the following equation:

$$H = \frac{1.257ni}{L} \quad (2)$$

where H is the magnetic field (measured in Oe), n , number of turns in a coil, i , the applied current and L , the diameter of a turn in cm. H values are found to be 168, 251 and 335 Oe (equivalent to 13, 20 and 27 kA m^{-1}) for 200, 300 and 400 A applied currents, respectively. The room temperature magnetizations of these samples were determined using a Vibrating Sample Magnetometer (VSM).

3. Results and discussion

3.1 XRD and TEM studies

Crystal structures of as-prepared core (3 at% Eu³⁺ doped CaMoO₄) and core@shell (shell: CaMoO₄) nanoparticles have been examined by an X-ray diffraction (XRD) method. Fig. 1 shows the XRD patterns of core and core@shell samples. As-prepared samples are well crystalline with tetragonal structure, and all peaks are matched with JCPDS card no. 29-0351. No extra impurity phases are detected. The standard diffraction pattern peaks are indexed to data with corresponding (hkl) planes between $15\text{--}80^\circ$. The average crystallite sizes calculated using Scherrer equation for as-prepared core and core@shell nanoparticles are found to be 24 and 27 nm, respectively. The unit cell parameters are found to be $a = 5.219 \text{ \AA}$, $c = 11.439 \text{ \AA}$ and $V = 311.60 \text{ \AA}^3$ for core and $a = 5.219 \text{ \AA}$, $c = 11.439 \text{ \AA}$ and $V = 311.62 \text{ \AA}^3$ for core@shell nanoparticles. These parameters are well matched with JCPDS card no. 29-0351 ($a = 5.226 \text{ \AA}$, $c = 11.430 \text{ \AA}$ and $V = 312.1 \text{ \AA}^3$). There is no significant change in lattice parameters and XRD patterns when an active core (Eu³⁺ doped) is covered with inactive shell (Eu³⁺ un-doped), *i.e.*, CaMoO₄:Eu³⁺@CaMoO₄. The micro-strain that is acting on both core and core@shell

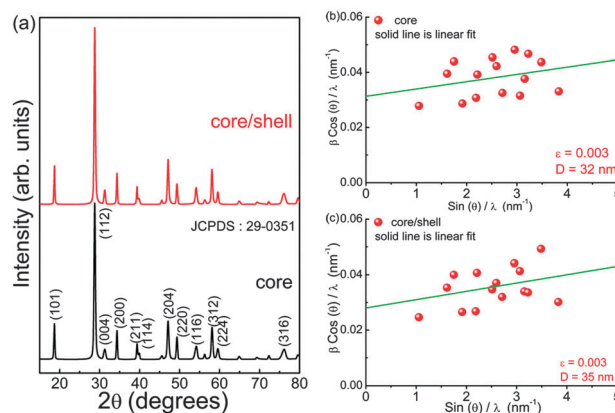


Fig. 1 (a) XRD patterns of the core (3 at% Eu³⁺ doped CaMoO₄) and core@shell (shell: CaMoO₄) as-prepared nanoparticles. The (hkl) planes are represented in the figure itself. The Williamson–Hall plots for the core (b) and core@shell (c) samples. Solid green line represents the linear fit to the experimental data. The micro-strain (ϵ_{hkl}) and effective crystallite sizes (D_{hkl}) are shown in the corresponding figures itself.

nanoparticles was analysed by the Williamson–Hall method.^{3,33} The Williamson–Hall equation can be represented as shown below:

$$\frac{\beta_{hkl} \cos \theta}{\lambda} = \frac{1}{D_{hkl}} + (\varepsilon_{hkl}) \frac{\sin \theta}{\lambda} \quad (3)$$

where β_{hkl} is the full width at half maxima (FWHM) of XRD patterns, θ is the diffraction angle, λ is the wavelength of the X-rays, D_{hkl} is the effective crystallite size and ε_{hkl} is the micro-strain. The instrumental broadening (ε_{inst}) is removed by using the Si standard, discussed in our earlier report.⁴ Fig. 1(b and c) shows the plot between $(\beta_{hkl} \cos(\theta))/\lambda$ and $\sin(\theta)/\lambda$ for the as-prepared core and core@shell samples. It is observed that the $(\beta_{hkl} \cos(\theta))/\lambda$ value increases with $\sin(\theta)/\lambda$. The data points are fitted with a linear equation. The micro-strain (ε_{hkl}) and effective crystallite (D_{hkl}) sizes calculated are shown in the figure itself. The average effective crystallite sizes calculated from the Williamson–Hall equation are 32 and 35 nm for core and core–shell samples, respectively, which are slightly more than those of Scherrer equation. However, we do not find any significant difference in ε_{hkl} (0.003) calculated for both core and core@shell within the span of the error bar. The effective crystallite size of the core@shell sample is slightly higher than a core sample. Positive slope values (ε_{hkl}) for both core and core@shell indicates tensile strain acting on the particle. Patra *et al.* recently reported tensile strain (positive slope) for SnO_2 nanoparticles and compressive strain (negative slope) for nanorods.³⁴ Sharma and co-workers recently reported a variation in strain (0.001–0.03) in Dy^{3+} doped CaMoO_4 . It is found that strain almost increases with an increase in Dy^{3+} concentration, and it is relaxed by co-doping of K^+ ions in CaMoO_4 .³⁵ TEM images of $\text{CaMoO}_4:\text{Eu}^{3+}$ and $\text{Fe}_3\text{O}_4\text{-CaMoO}_4:\text{Eu}$ are shown in Fig. 2. The particles are found to be spherical and sizes of 30–40 nm are observed.

3.2 Raman study

Fig. 3 shows the Raman scattering spectra of the core (3 at% Eu^{3+} doped CaMoO_4) and core@shell (shell: CaMoO_4) as-prepared nanoparticles recorded at room temperature. The Scheelite structure shows 26 modes of vibrations ($3A_g, 5A_u, 5B_g, 3B_u, 5E_g, 5E_u$) in which 13 modes are Raman active ($3A_g, 5B_g, 5E_g$) and ($4A_u, 4E_u$) are IR active.^{36,37} The Fourier transform infrared (FTIR) spectra of the core are discussed in our earlier study.⁴ The observed Raman peaks are given in Table 1 and compared with the reported values. Among all Raman peaks, the peak at $\sim 876 \text{ cm}^{-1}$ shows the highest intensity having (full width at half maximum) FWHM $\sim 12 \text{ cm}^{-1}$. The four Raman bands below 267 cm^{-1} are due to external modes (lattice modes) whereas the five bands below 910 cm^{-1} correspond to internal/optical modes (within MoO_4^{2-}).³⁸ We do not find significant changes in Raman peak positions of the core sample as compared to the core@shell sample. The ratio of integrated intensities of external mode (199 cm^{-1}) to internal mode (320 cm^{-1}) is found to be 0.42 and 0.46 for core and core@shell samples, respectively. The Raman spectra of both core and core@shell samples are normalised to their maximum peak intensity at 876 cm^{-1} . It is found that the Raman modes at $\sim 320, 389$ and 791 cm^{-1} show a significant change in emission intensity as compared to other Raman modes. On clear observation, the integrated intensity of the $\sim 320 \text{ cm}^{-1}$ peak for the core sample is ~ 1.1 times

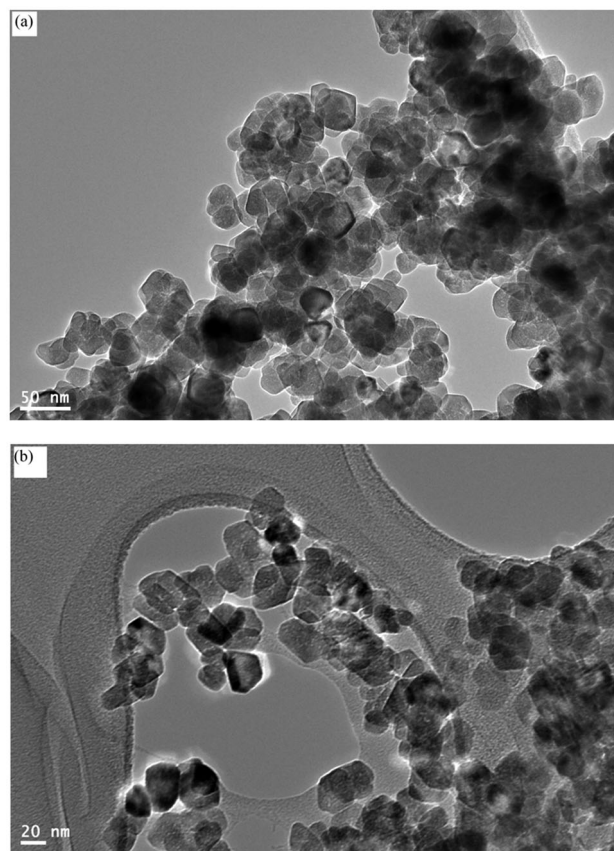


Fig. 2 TEM images of (a) $\text{CaMoO}_4:\text{Eu}^{3+}$ @ CaMoO_4 and (b) $\text{Fe}_3\text{O}_4\text{-CaMoO}_4:\text{Eu}$.

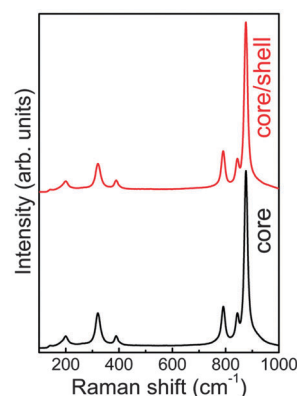


Fig. 3 Raman spectra of core (3 at% Eu^{3+} doped CaMoO_4) and core–shell (shell: CaMoO_4) as-prepared nanoparticles.

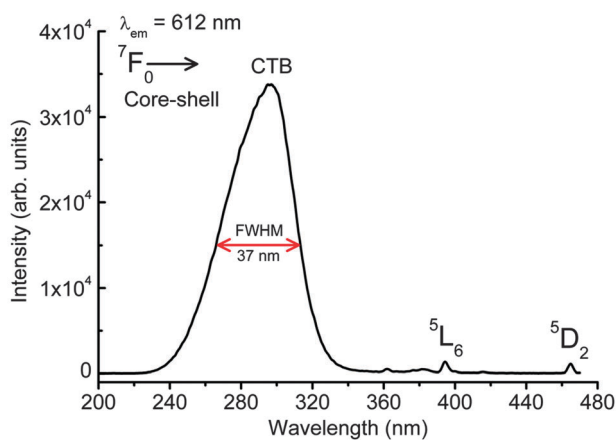
that of the core@shell sample and peaks are symmetric with Lorentzian fitting. In the case of the $\sim 791 \text{ cm}^{-1}$ peak, the intensity of the core sample is 0.98 times that of the core@shell sample.

3.3 Luminescence study

3.3.1 Emission and excitation studies. Fig. 4 shows the excitation spectra of the as-prepared 3 at% Eu^{3+} doped CaMoO_4 core@shell nanoparticles by monitoring emission at $\sim 612 \text{ nm}$. A xenon lamp (450 W) was used as the excitation source.

Table 1 The Raman peak assignment of the as-prepared core and core@shell nanoparticles

Raman modes	Observed peak position (cm ⁻¹)		Reported peak position (cm ⁻¹)	
	Core	Core@shell	Ref. 36	Ref. 38
B _g	—	86	83	—
E _g	115	112	110	111.5
E _g	141	141	141	143
E _g	199	199	201	189.5
A _g	320	321	322	321.5
B _g	389	390	390	391
E _g	791	791	793	792
B _g	844	844	845	845
A _g	876	876	878	877

**Fig. 4** Excitation spectrum of the as-prepared 3 at% Eu³⁺ doped CaMoO₄ core-shell nanoparticles by monitoring emission at 612 nm. Excitation source is from a xenon lamp (450 W).

The broad absorption peak appeared in between 220 to 350 nm having a peak maximum at ~300 nm and the full width at half maximum (FWHM) of ~37 nm is assigned to O → Mo charge transfer band (Mo–O CTB).^{7,39} The Mo–O CTB is asymmetric. After deconvolution, two peaks were found at 275 and 301 nm. The former is related to the Eu–O CTB band and the latter one is related to Mo–O CTB. The two sharp peaks at ~394 and 464 nm can be assigned to the ⁷F₀ → ⁵L₆ and ⁷F₀ → ⁵D₂ transitions of Eu³⁺, respectively.⁴ Typically, the intensity of Mo–O CTB is ~228 times stronger than that of the ⁷F₀ → ⁵L₆ transition. The formation of a shell over a core significantly enhances the absorption intensity of Mo–O CTB.

Fig. 5(a) shows the emission spectra of Eu³⁺ doped CaMoO₄ (Eu³⁺ = 1, 3, 5, 7, 10, 15, 20 and 30 at%) as-prepared samples. The excitation wavelength is 266 nm (corresponding to Eu–O CTB) with a Nd-YAG laser. It consists of four characteristic emission peaks at 591, 612, 652 and 700 nm which are assigned to the ⁵D₀ → ⁷F₁, ⁵D₀ → ⁷F₂, ⁵D₀ → ⁷F₃ and ⁵D₀ → ⁷F₄ transitions of the Eu³⁺ ion, respectively.⁴⁰ The highest intensity peak is found at 612 nm (⁵D₀ → ⁷F₂), and this can be assigned to the electric dipole allowed transition (Δ*j* = 2). The transition observed at 591 nm (⁵D₀ → ⁷F₁) is due to the magnetic dipole allowed transition of the Eu³⁺ ion (Δ*j* = 1). The electric dipole

transition ⁵D₀ → ⁷F₂ is hypersensitive whereas magnetic dipole transition ⁵D₀ → ⁷F₁ is insensitive to the crystal field environment around the Eu³⁺ ion. Magnetic dipole transition is dominant when Eu³⁺ ions occupy the site with inversion symmetry. In the other case electric dipole transition will be dominating according to Judd–Ofelt theory.⁴¹ Based on the crystal structure of CaMoO₄ (tetragonal structure with space group *I*_{41/a}), the Eu³⁺ ion has 8 O²⁻ ions to form a EuO₈ polyhedron, in which there are two different Eu–O bond lengths and therefore, EuO₈ is asymmetric. It is expected that the luminescence intensity for the electric dipole transition will be more than that of the magnetic dipole transition.⁴² The change in Ca/Eu–O bond length with Eu³⁺ ion dopant concentration was confirmed by Rietveld refinement of the XRD data in our earlier work.⁴ The luminescence intensity of the transition/curve is calculated after fitting with the Gaussian distribution function

$$I = I_b + \sum_{i=1}^n \frac{A_i}{w_i \sqrt{\pi/2}} e^{-\frac{2(\lambda - \lambda_{ci})^2}{w_i^2}} \quad (4)$$

where *I* is the intensity, *I_b* is the background intensity, *w_i* is the FWHM of the curve, *A_i* is the area under the curve, *λ* is the wavelength and *λ_{ci}* is the mean value corresponding to the transition. These are fitted in the range 583–600 and 600–628 nm for the ⁵D₀ → ⁷F₁ and ⁵D₀ → ⁷F₂ transitions, respectively. A typical fitting to the electric and magnetic dipole transitions data for the as-prepared 1 at% Eu³⁺ doped CaMoO₄ is shown in Fig. S1 (see ESI†). The fitting has been carried out after the baseline correction (*I_b* = 0). The parameters obtained after fittings are given in the figure itself with goodness of a parameter (*χ*² = 0.99205). In the case of the as-prepared samples, the integrated luminescence intensity of the electric dipole transition ⁵D₀ → ⁷F₂ (*A*₂₁) decreases with the increase of Eu³⁺ concentration due to concentration quenching effect (Fig. 6a). The variation of FWHM (*w*₂) with Eu³⁺ concentration is shown in Fig. 6b. The *w*₂ increases with Eu³⁺ concentrations up to 10 at%.

The structural distortion around the Eu³⁺ ion is estimated by the ratio of an integrated area of electric dipole transition to magnetic dipole transition, which is known as the asymmetric ratio (*A*₂₁):

$$A_{21} = \frac{\int_{583}^{628} I_2 d\lambda}{\int_{583}^{600} I_1 d\lambda} \quad (5)$$

The *A*₂₁ of as-prepared sample decreases from 11 to 5.6 with an increase of Eu³⁺ concentration up to 30 at% (Fig. 6c).

The emission spectra of samples annealed at 500 °C after excitation at 266 nm is shown in Fig. 5b. The *A*₂ increases as Eu³⁺ concentration increases from 1 to 3 at% and then decreases significantly with increasing Eu³⁺ concentration. The optimum intensity is more than that of the as-prepared sample due to the extent of reduction of non-radiative channels on annealing (Fig. 6a). The *w*₂ increases with increasing Eu³⁺ concentration (Fig. 6b). The *A*₂₁ is found to be in range of 8.8–13.3 (Fig. 6c).

The samples annealed at 900 °C show intense emission on excitation at 266 nm (Fig. 5c). The *A*₂ value increases as Eu³⁺

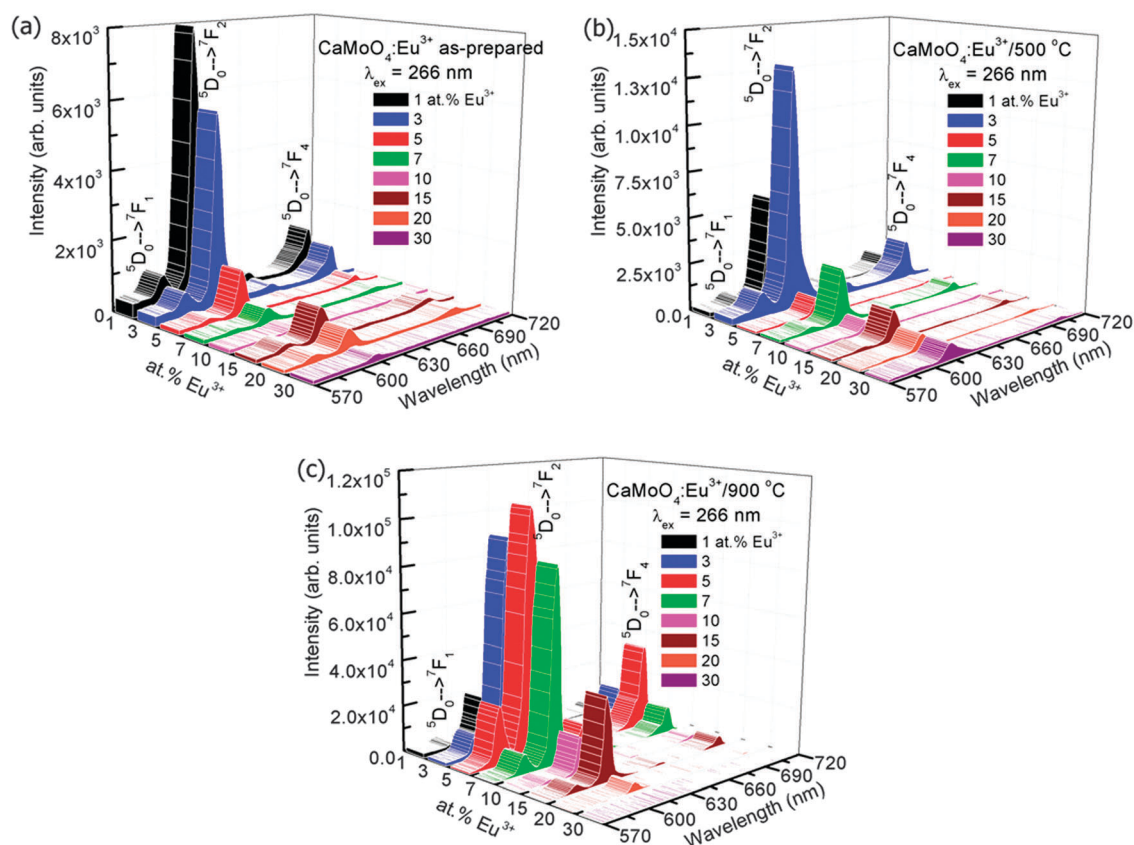


Fig. 5 Emission spectra of Eu^{3+} doped CaMoO_4 ($\text{Eu}^{3+} = 1, 3, 5, 7, 10, 15, 20$ and 30 at%) under 266 nm excitation of (a) as-prepared, (b) 500 and (c) 900 °C annealed nanoparticles. Excitation source is from a Nd-YAG laser.

concentration increases from 1 to 5 at% and then decreases with a further increase of Eu^{3+} concentration (Fig. 6a) and is more than that of the as-prepared and 500 °C annealed samples due to the extent of reduction of a non-radiative process with annealing. The surface of the particles is contributing to a non-radiative probability. In the as-prepared samples, particle size is small and the surface has H_2O and EG, which act as a quencher for luminescence. When the samples are annealed at 500 °C, the decomposition of EG occurs. Most carbon impurities and H_2O are removed. Furthermore, the particle size increases. This gives an enhancement in luminescence intensity. A significant improvement in luminescence can be observed for the 900 °C annealed sample because the quenching centres H_2O and surface dangling bonds are minimum (Fig. 5c). The w_2 increases initially up to 5 at% Eu^{3+} and decreases with increasing Eu^{3+} concentration (Fig. 6b) and is less than that of the as-prepared or 500 °C annealed sample. The A_{21} is found to be in range of ~ 7.7 – 10.5 (Fig. 6c), which is still quite high. Reported A_{21} values are found to be in the range of ~ 7.4 – 7.9 on excitation to Mo–O/Eu–O CTB in Eu^{3+} doped CaMoO_4 (260 nm, xenon lamp excitation).⁴³ We also found A_{21} values to be in the range of 7 – 9 under xenon lamp excitation of 150 W.³⁹ A higher asymmetric ratio indicates the increase of occupancy of Eu^{3+} in Ca^{2+} sites without inversion symmetry. In addition, Raju and co-workers⁷ reported a high asymmetric

ratio ~ 10 ($\text{CaMoO}_4:\text{Eu}$). This may be due to the polarization effect of the MoO_4 cluster in the CaMoO_4 host.³⁹ To understand the effect of pump power on A_{21} , 900 °C annealed 3 at% Eu^{3+} doped CaMoO_4 samples were excited with 532 nm laser excitation ($^5\text{D}_1$ level, Fig. 7a).

Fig. 7b shows the variation in A_{21} , integrated intensity of electric and magnetic dipole transitions at different pump powers of a 532 nm laser. The A_{21} value decreases from 12 to 7 as the power increases from 0.1 to 2 W, whereas the integrated intensity of the peaks increases up to an optimum power of 1 W. The decrease in emission intensity at a higher power density above 1 W may be due to temperature generated in the sample. An increase in temperature in the sample will increase the fluctuation in luminescence intensity. However, the variation of A_{21} values with the intensity of excitation photons has not been reported to the best of authors' knowledge.

Fig. 8(a and b) shows the emission spectra of the as-prepared 3 at% Eu^{3+} doped CaMoO_4 core and core@shell nanoparticles under different excitation wavelengths (Xe-lamp source, 450 W). Here the shell is inactive (CaMoO_4). Core nanoparticles show optimum emission near 266 nm excitation whereas the core@shell nanoparticles show optimum emission at ~ 300 nm excitation. This is due to a shift of Mo–O CTB to a higher wavelength region. A similar observation of an increase of the V–O CTB (CTB = charge transfer band) to the higher wavelength

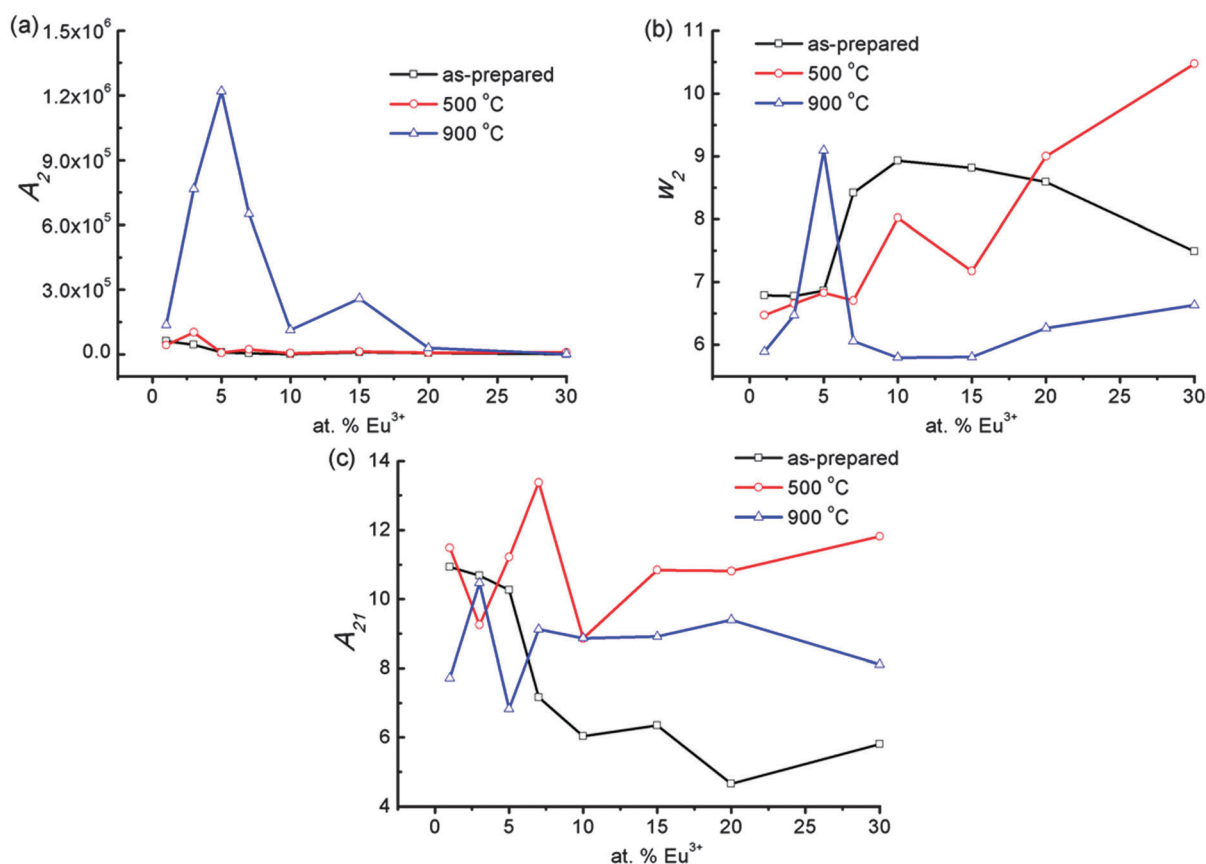


Fig. 6 (a) Integrated area of the $^5D_0 \rightarrow ^7F_2$ transition ($\int ^5D_0 \rightarrow ^7F_2$) and (b) the corresponding FWHM of Eu³⁺ doped CaMoO₄ (Eu³⁺ = 1, 3, 5, 7, 10, 15, 20 and 30 at%) under 266 nm excitation of as-prepared, 500 and 900 °C annealed nanoparticles. (c) Their corresponding asymmetric ratio ($A_{21} = \int ^5D_0 \rightarrow ^7F_2 / \int ^5D_0 \rightarrow ^7F_1$). Excitation source is from a Nd-YAG laser.

after core-shell formation (core: YVO₄:Eu and core-shell: YVO₄:Eu@YVO₄) have been reported.⁴⁴ The luminescence spectra of core and core@shell nanoparticles show similar nature between 570–700 nm having a strong emission peak at ~615 nm ($^5D_0 \rightarrow ^7F_2$). Typical emission intensity of core@shell nanoparticles at 300 nm excitation is ~10 times higher than core nanoparticles. This is due to the removal of dangling bonds on the surface of the active core by the inactive shell. Moreover, these nanoparticles are highly dispersible in water. This may be due to the interaction of EG present on the surface of nanoparticles with H₂O.

3.3.2 Effect of host sensitizer. CaMoO₄ nanoparticles show a broad absorption band in ~200–350 nm. This is related to Mo–O CTB of host (CaMoO₄). Upon excitation at 260–300 nm, it shows the emission spectrum in 320–650 nm.^{7,39} Also, absorption band of Eu–O CTB occurs in 230–260 nm in most hosts doped with Eu³⁺.^{45,46} Thus excitation at 266 nm is related to Mo–O/Eu–O CTB. This broad-band light emitted from host (CaMoO₄ or Eu–O CTB) in 320–650 nm is absorbed by Eu³⁺ ions in the ground state ($^7F_0 \rightarrow ^5L_6$ at 395 nm and $^7F_0 \rightarrow ^5D_2$ at 465 nm) and thereby enhancement of Eu³⁺ emission occurs.^{47,48} The energy transfer from the host (as sensitizer) to an activator will depend on the overlapping of an energy

band of the host (CaMoO₄) emitting light with the activator (Eu³⁺) absorption. This is schematically shown in Fig. 9.

3.3.3 Induction heating of hybrid MN. The heat-generation from hybrid Fe₃O₄–CaMoO₄:Eu MN is studied using an induction heating setup on applying different input currents 200, 300 and 400 A. 1 mL of dispersed hybrid MN in water is placed in an induction heating setup coupled with temperature sensing optical fibre thermocouple. Fig. 10(a) shows the digital photograph of induction heating coil used in the experiment, and Fig. 10(b) shows their temperature kinetics curves of the sample (32 mg/1 mL). Here PEG solution (100 mg of polyethylene 6000 in 100 mL distilled water) is used as the medium. It is shown that temperature rises with an increase in time and current. Hybrid MN achieves ~42 °C temperature in 9 min for 300 A and 4.3 min for 400 A applied current, whereas temperature attained is below 36 °C for 200 A current in 10 min. The PEG coated over the surface of hybrid nanoparticles makes the nanoparticles more dispersible. In general pure Fe₃O₄ MN (10 mg mL⁻¹, medium is sodium carbonate) shows high induction heating ability (~60 °C in 10 min at 265 kHz frequency and 400 A (*i.e.*, 335 Oe)), reported in our earlier study.⁴⁹ The rise in temperature is also controlled by the amount of Fe₃O₄ nanoparticles as well as the applied field at

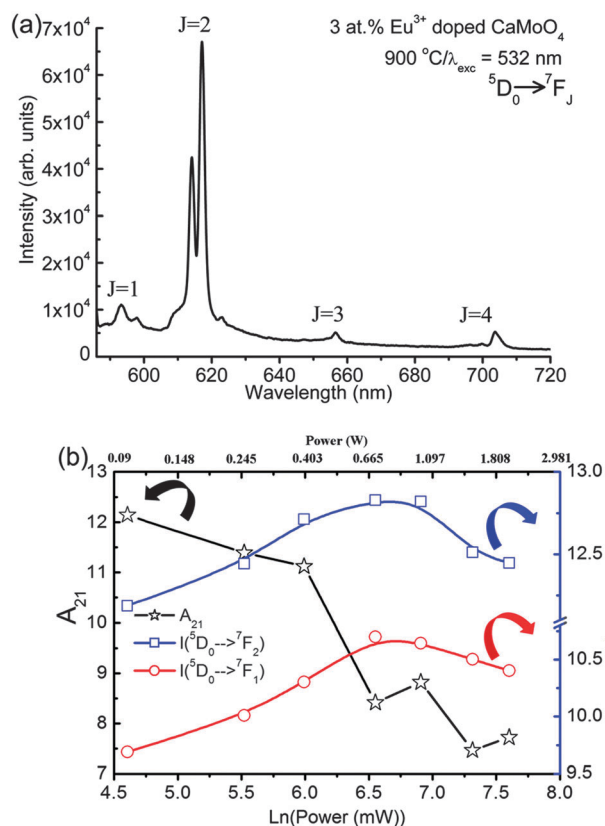


Fig. 7 (a) Typical emission spectrum of 900 °C annealed 3 at% Eu^{3+} doped CaMoO_4 nanoparticles under 532 nm laser excitation, (b) variation in A_{21} , electric and magnetic dipole transition intensities of 900 °C annealed 3 at% Eu^{3+} doped CaMoO_4 nanoparticles with different powers (P) of a 532 nm laser.

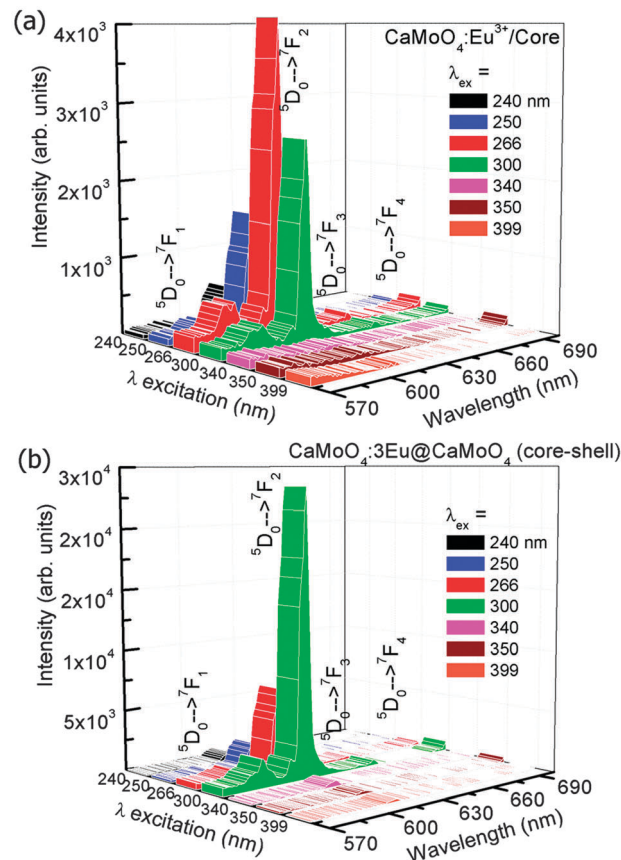


Fig. 8 Emission spectra of Eu^{3+} doped CaMoO_4 ($\text{Eu}^{3+} = 1, 3, 5, 7, 10, 15, 20$ and 30 at%) of the as-prepared (a) core and (b) core@shell nanoparticles under different excitation wavelengths. Excitation source is from a xenon lamp (450 W).

a particular frequency. The temperature required for hyperthermia application for killing the cancer tissues is ~ 42 °C.⁴⁹ The specific absorption rate (SAR) of hybrid MN is calculated by using following relationship:

$$\text{SAR} = C(\Delta T/\Delta t)(1/m_{\text{mag}}) \quad (6)$$

where C is the sample-specific heat capacity and $\Delta T/\Delta t$ is the initial slope of the time-dependent temperature curve. The value of m_{mag} is considered as the amount of magnetite or Fe per total amount of magnetite or Fe and water. The value of $\Delta T/\Delta t$ is calculated in the range 0–5 min. Here the volume of water was 1 mL, which is equal to 1 g. 1 mL of $\text{Fe}_3\text{O}_4\text{-CaMoO}_4\text{:Eu}$ contains 7.2 mg (Fe_3O_4) and 25 mg of $\text{CaMoO}_4\text{:Eu}$. The SAR values are found to be 10, 19 and 26 W g^{-1} for 200, 300 and 400 A applied current, respectively. These SAR values are comparable with reported values.⁴⁹ $\text{Fe}_3\text{O}_4\text{-CaMoO}_4\text{:Eu}$ hybrid nanoparticles are effectively used for hyperthermia applications. Fig. 11 gives the magnetization vs. magnetic field (H) of hybrid ($\text{Fe}_3\text{O}_4\text{-CaMoO}_4$) at 300 K. There is no coercivity indicating superparamagnetism. Magnetization at 2 Tesla is ~ 14.2 emu g^{-1} . This value includes CaMoO_4 also. Ratio of CaMoO_4 to Fe_3O_4 is 4 : 1. Thus magnetization per 1 g of Fe_3O_4 is ~ 63 emu. Magnetization of pure Fe_3O_4 is ~ 60 emu g^{-1} .²²

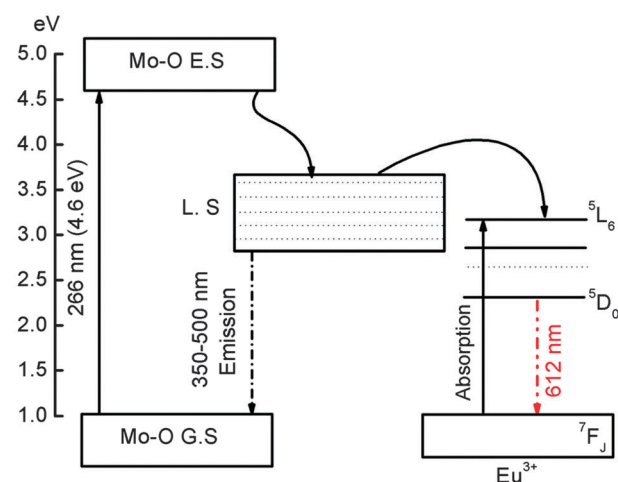


Fig. 9 Schematic energy diagram of absorption, emission bands of Mo–O CT and Eu^{3+} and the energy transfer (ET) process.

Enhancement in magnetization is related to an increase in crystalline anisotropic (K) in the hybrid due to the addition of 4f orbitals of Eu^{3+} in the hybrid.

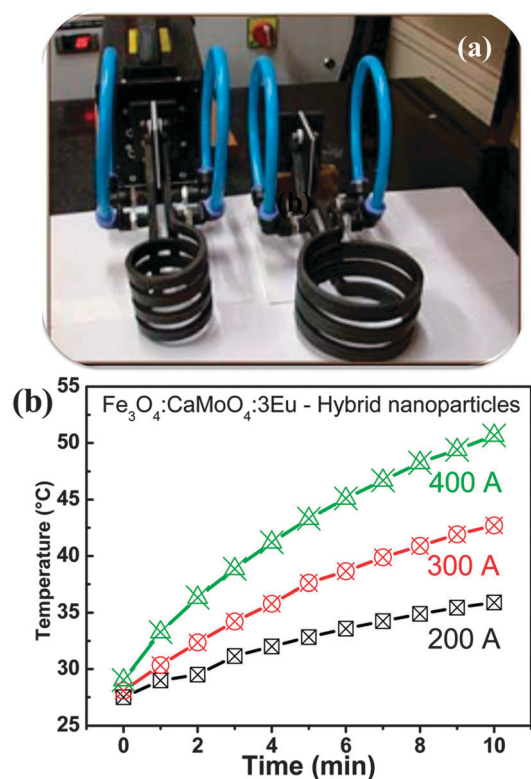


Fig. 10 (a) Digital photograph of induction heating system and (b) temperature attained vs. time at different alternative currents (200, 300 and 400 A) for $\text{Fe}_3\text{O}_4\text{-CaMoO}_4\text{:3Eu}$ hybrid magnetic nanoparticles in the induction coil.

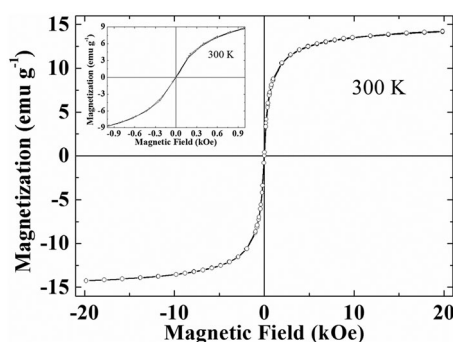


Fig. 11 Magnetization (M) versus applied magnetic field (H) curve for $\text{Fe}_3\text{O}_4\text{-CaMoO}_4\text{:3Eu}$ hybrid magnetic nanoparticles.

3.4 Luminescence of hybrid nanoparticles

Fig. 12 shows the emission spectrum of $\text{Fe}_3\text{O}_4\text{-CaMoO}_4\text{:Eu}$ (3 at%) hybrid nanoparticles under 250 nm excitation (xenon lamp 450 W) and 398 nm excitation (not shown). It shows strong red emission at ~ 612 nm which is assigned to the $^5\text{D}_0 \rightarrow ^7\text{F}_2$ transition of the Eu^{3+} ion. Moreover, the emission intensity of hybrid nanoparticles is slightly less than the pure $\text{CaMoO}_4\text{:Eu}$ sample. This may be due to the presence of less number of Eu^{3+} ions per unit mass of sample and also magnetic nanoparticles quench luminescence intensity.

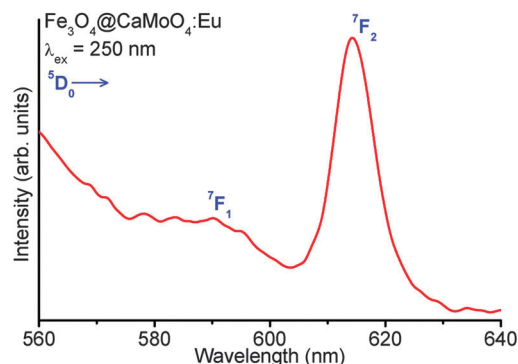


Fig. 12 Luminescence spectrum of $\text{Fe}_3\text{O}_4\text{@CaMoO}_4\text{:3Eu}$ hybrid magnetic nanoparticles under 250 nm excitation.

3.5 *In vitro* cytotoxicity (MTT assay) of $\text{Fe}_3\text{O}_4\text{-CaMoO}_4\text{:Eu}$ hybrid nanoparticles

To provide comprehensive results about the potential applications of synthesized $\text{Fe}_3\text{O}_4\text{-CaMoO}_4\text{:Eu}$ (3 at%) hybrid magnetic nanoparticles for non-invasive imaging purposes, it is essential to measure the cytotoxicity of the synthesized nanoparticles. The cellular cytotoxicity profiles of the $\text{Fe}_3\text{O}_4\text{-CaMoO}_4\text{:Eu}$ hybrid magnetic nanoparticles are determined on two type cell lines, human hepatoblastoma (HepG2) and hTERT cells, using a MTT assay. As shown in Fig. 13 and 14, the cells are treated with different concentrations of $\text{Fe}_3\text{O}_4\text{-CaMoO}_4\text{:Eu}$ hybrid magnetic nanoparticles for 24 h, to determine the effect of concentration of the nanoparticles. The viability of non-treated cells is assumed to be 100%. On incubation of the HepG2 cells with the $\text{Fe}_3\text{O}_4\text{-CaMoO}_4\text{:Eu}$ hybrid magnetic nanoparticles for 24 h at a concentration of $5 \mu\text{g mL}^{-1}$ it shows little change in cell viability. Whereas the cells exposed to increasing concentrations ($5, 10, 20, 40, 80, 160, 320$ and $640 \mu\text{g mL}^{-1}$) of $\text{Fe}_3\text{O}_4\text{-CaMoO}_4\text{:Eu}$ hybrid magnetic nanoparticles for 24 h show a noticeable dose-dependent decrease in their relative cell viability. The IC_{50} value ($\text{Fe}_3\text{O}_4\text{-CaMoO}_4\text{:Eu}$ inhibits the

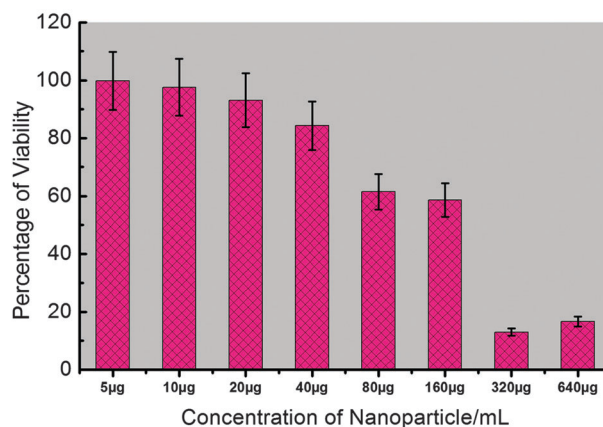


Fig. 13 Cytotoxicity of $\text{Fe}_3\text{O}_4\text{-CaMoO}_4\text{:Eu}$ hybrid magnetic nanoparticles against HepG2 cells determined by MTT assay after 24 h of treatment. IC_{50} was determined as $193.26 \mu\text{g mL}^{-1}$. Error bars represent standard deviation ($n = 3$).

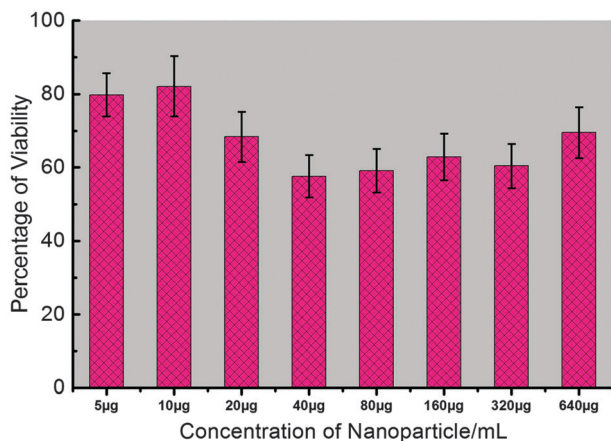


Fig. 14 Cytotoxicity of $\text{Fe}_3\text{O}_4\text{-CaMoO}_4\text{:Eu}$ hybrid magnetic nanoparticles against hTERT 20 cells determined by MTT assay after 24 h of treatment. IC_{50} was not achieved by the tested doses range (5–640 $\mu\text{g mL}^{-1}$). Error bars represent standard deviation ($n = 3$).

50% cell viability) of the $\text{Fe}_3\text{O}_4\text{-CaMoO}_4\text{:Eu}$ hybrid magnetic nanoparticles is calculated to be approximately $193.26 \mu\text{g mL}^{-1}$.

The toxic effect of $\text{Fe}_3\text{O}_4\text{-CaMoO}_4\text{:Eu}$ hybrid magnetic nanoparticles on cell viability was also assessed on a second cell line, hTERT cells (human mesenchymal stem cells). This assay is used to assess the viability of the hTERT cell line after exposure of $\text{Fe}_3\text{O}_4\text{-CaMoO}_4\text{:Eu}$ hybrid magnetic nanoparticles at various concentrations for 24 h. As is evident from Fig. 14, in general, the $\text{Fe}_3\text{O}_4\text{-CaMoO}_4\text{:Eu}$ hybrid magnetic nanoparticles show no significant dose-dependent cytotoxic effects even at higher concentrations. About 60–80% cells are viable when compared to the control. These results confirmed the non-toxic nature of $\text{Fe}_3\text{O}_4\text{-CaMoO}_4\text{:Eu}$ hybrid magnetic nanoparticles in the *in vitro* model. In other words, these composite nanoparticles had better biocompatibility in *in vitro* cell assays. The results of this study are in agreement with the current fact that the most often used biocompatible material for the preparation of magnetic particles is the iron oxide magnetite. Interestingly, $\text{Fe}_3\text{O}_4\text{-CaMoO}_4\text{:Eu}$ exert a mild toxicity (75% viability at the highest concentration) on a normal cell line hTERT, whereas HepG2 cells (a cancerous cell line) show their sensitivity against the same hybrid-nanocomposite. Therefore, it is suggested that the acute cytotoxicity primarily is originated from the cellular internalization of $\text{Fe}_3\text{O}_4\text{-CaMoO}_4\text{:Eu}$ hybrid magnetic nanoparticles rather than physical damage on the cellular membrane. Moreover, it has been proven by previous studies that nanoparticles can cross the cell membrane and enter the cytoplasm through several different routes.^{50,51} A recent study demonstrated that the cellular response of human foreskin fibroblasts is different for the different morphologies of composite nanoparticles, with spherical particles exhibiting no cytotoxicity, rod-like particles increasing cell proliferation, and platelet particles being markedly cytotoxic.⁵⁰ Once a metal present in the particle has penetrated the cells, metal ions can leach from the particle and generate reactive oxygen species (ROS) in the cell interior leading to oxidative stress to cells, in what is called a “Trojan horse” mechanism.^{52,53}

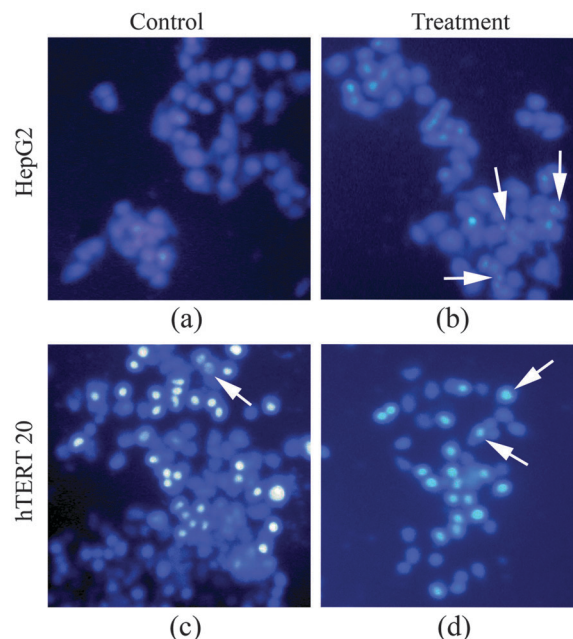


Fig. 15 Microscopic visualizations of HepG2 and hTERT 20 cells after staining with fluorescent (DAPI) dye, (a & c) are untreated controlled cells of HepG2 and hTERT 20 cells and (b & d) are treated with $\text{Fe}_3\text{O}_4\text{-CaMoO}_4\text{:Eu}$ hybrid magnetic nanoparticles.

The toxicological effects of $\text{Fe}_3\text{O}_4\text{-CaMoO}_4\text{:Eu}$ hybrid magnetic nanoparticles are also monitored by analyzing the morphology of cells. The $\text{Fe}_3\text{O}_4\text{-CaMoO}_4\text{:Eu}$ hybrid magnetic nanoparticles are treated with HepG2 and hTERT cell lines. An inverted optical microscope is used to examine the alteration in cell morphology between treated and non-treated hybrid magnetic nanoparticles (Fig. 15). The cells are grown with normal colonies-like morphologies after co-labelling with the $\text{Fe}_3\text{O}_4\text{-CaMoO}_4\text{:Eu}$ hybrid magnetic nanoparticles and DAPI for cell nuclei counterstaining. The fluorescence images demonstrate that the $\text{Fe}_3\text{O}_4\text{-CaMoO}_4\text{:Eu}$ hybrid magnetic nanoparticles are clearly adsorbed onto the membrane and internalized into the cytoplasm of the cells, particularly with relatively light blue (Fig. 15) luminescence. It is found that the control cells are healthy and start to proliferate and gradually grew to form small colonies (Fig. 15(a and c)), however, the treated hTERT cells are rounded off and formed clusters (Fig. 15(d)). It shows no significant cell death and no change in cell morphology as observed on microscopic examinations of cells during the period of study. These results indicate that the viability of the hTERT cells is not affected by the presence of the above samples, suggesting that they are quite biocompatible. In addition, there is no nuclear fragmentation (HepG2 cells formed colonies) when cells are treated with $\text{Fe}_3\text{O}_4\text{-CaMoO}_4\text{:Eu}$ hybrid magnetic nanoparticles (Fig. 15(b)). It is seen that the control cells do not show any fluorescence whereas the cells treated with $\text{Fe}_3\text{O}_4\text{-CaMoO}_4\text{:Eu}$ hybrid magnetic nanoparticles show strong luminescence, which shows its potential to label hTERT cells for bioimaging. The present study is to give an overall toxic response idea of the $\text{Fe}_3\text{O}_4\text{-CaMoO}_4\text{:Eu}$ hybrid magnetic nanoparticles. Interestingly, $\text{Fe}_3\text{O}_4\text{-CaMoO}_4\text{:Eu}$ hybrid

magnetic nanoparticles are found potentially toxic for a cancer cell line (HepG2) and to a large extent non-toxic for a normal cell line (hTERT). It advocates the potentiality of the nanoparticles to be used as an anticancer drug vehicle. However, the confocal fluorescence microscopy imaging, genotoxic response experiments and their detailed toxic potentiality with other cancer and normal cell lines are currently underlying. These will be the subject of future investigations.

4. Conclusions

CaMoO₄:Eu³⁺ ions (Eu³⁺ = 1, 3, 5, 7, 10, 15, 20 and 30 at%) and 3 at% Eu³⁺ doped CaMoO₄ core@shell nanoparticles have been prepared using urea hydrolysis in ethylene glycol medium at 150 °C. The emission intensity of Eu³⁺ doped CaMoO₄ (core) nanoparticles is significantly enhanced by forming an inactive shell (CaMoO₄) on the core. In the case of the as-prepared samples, the emission intensity of core@shell nanoparticles is ~10 times higher than that of core nanoparticles on 300 nm excitation. The effect of pump power on the asymmetric ratio (*A*₂₁) has been studied. It is found that *A*₂₁ values under laser excitation are slightly higher than xenon lamp excitation as a source. Also, increase in pump power enhances the *A*₂₁ up to optimum power and then decreases. The prepared nanoparticles show high dispersibility in water. The hybrid Fe₃O₄-CaMoO₄:Eu MN can attain hyperthermia temperature (42 °C) and give luminescence in the red region, which lies in the biological window. The cell viability and proliferation test on hTERT cells indicated that Fe₃O₄-CaMoO₄:Eu hybrid nanoparticles are less toxic or antiproliferative effects in the cell cultures, whereas the cell viability on HepG2 cells are reduced and showed the toxic effects. So they can be a potential candidate for optical imaging, biological, hyperthermia and optoelectronic applications.

Acknowledgements

This work has been sponsored by the University Grants Commission (UGC) under Dr D. S. Kothari Postdoctoral Fellowship Scheme (No. F.4-2/2006(BSR)/13-309/2008(BSR)) to Dr A. K. Parchur. AKP and RSN thank Dr S. M. Yusuf, Solid State Physics Division, BARC, Mumbai for providing Magnetic data.

References

- 1 R. S. Ningthoujam, in *Enhancement of luminescence by rare earth ions doping in semiconductor host*, ed. S. B. Rai and Y. Dwivedi, Nova Science Publishers Inc, USA, 2012, ch. 6, pp. 145–182.
- 2 P. Ghosh, J. Oliva, E. D. Rosa, K. K. Haldar, D. Solis and A. Patra, *J. Phys. Chem. C*, 2008, **112**, 9650.
- 3 A. Kar, A. Datta and A. Patra, *J. Mater. Chem.*, 2010, **20**, 916.
- 4 A. K. Parchur and R. S. Ningthoujam, *Dalton Trans.*, 2011, **40**, 7590.
- 5 C. N. R. Rao, H. S. S. R. Matte, R. Voggu and A. Govindaraj, *Dalton Trans.*, 2012, **41**, 5089.
- 6 A. A. Ansari, M. Alam, J. P. Labis, S. A. Alrokayan, G. Shafi, T. N. Hasan, N. A. Syed and A. A. Alshatwi, *J. Mater. Chem.*, 2011, **21**, 19310.
- 7 G. S. R. Raju, E. Pavitra, K. Y. Hwan and Y. J. Su, *J. Mater. Chem.*, 2012, **22**, 15562.
- 8 A. A. Ansari, S. P. Singh, N. Singh and B. D. Malhotra, *Spectrochim. Acta, Part A*, 2012, **86**, 432.
- 9 S. Vidya, S. Solomon and J. K. Thomas, *Phys. Status Solidi A*, 2012, **209**, 1067.
- 10 J. H. Chung, J. H. Ryu, S. W. Mhin, K. M. Kim and K. B. Shim, *J. Mater. Chem.*, 2012, **22**, 3997.
- 11 L. Tong, J. Shi, D. Liu, Q. Li, X. Ren and H. Yang, *J. Phys. Chem.*, 2012, **116**, 7153.
- 12 A. K. Parchur, A. I. Prasad, A. A. Ansari, S. B. Rai and R. S. Ningthoujam, *Dalton Trans.*, 2012, **41**, 11032.
- 13 C. W. Raubach, M. Z. Krolow, M. F. Mesko, S. Cava and M. L. Moreira, *CrystEngComm*, 2012, **14**, 393.
- 14 F. Wang, R. Deng, J. Wang, Q. Wang, Y. Han, H. Zhu, X. Chen and X. Liu, *Nat. Mater.*, 2011, **10**, 1.
- 15 A. K. Parchur and R. S. Ningthoujam, *RSC Adv.*, 2012, **2**, 10854.
- 16 X. Ju, X. Li, Y. Yang, W. Li, C. Tao and W. Feng, *J. Solid State Chem.*, 2012, **187**, 109.
- 17 I. L. V. Rosa, L. H. Oliveira, E. Longo and J. A. Varela, *J. Fluoresc.*, 2011, **21**, 975.
- 18 Z.-L. Wang, R. Guo, G.-R. Li, L.-X. Ding, Y.-N. Ou and Y.-X. Tong, *RSC Adv.*, 2011, **1**, 48.
- 19 S. Zhou, Q. Chen, X. Hu and T. Zhao, *J. Mater. Chem.*, 2012, **22**, 8263.
- 20 X. L. Liu, H. M. Fan, J. B. Yi, Y. Yang, E. S. G. Choo, J. M. Xue, D. D. Fan and J. Ding, *J. Mater. Chem.*, 2012, **22**, 8235.
- 21 L. Zhou, J. Yuan and Y. Wei, *J. Mater. Chem.*, 2011, **21**, 2823.
- 22 R. Ghosh, L. Pradhan, Y. P. Devi, S. S. Meena, R. Tewari, A. Kumar, S. Sharma, N. S. Gajbhiye, R. K. Vatsa, B. N. Pandey and R. S. Ningthoujam, *J. Mater. Chem.*, 2011, **21**, 13388.
- 23 M. Jeun, S. Lee, J. K. Kang, A. Tomitaka, K. W. Kang, Y. I. Kim, Y. Takemura, K.-W. Chung, J. Kwak and S. Bae, *Appl. Phys. Lett.*, 2012, **100**, 092406.
- 24 T. T. T. Mai, P. T. Ha, H. N. Pham, T. T. H. Le, H. L. Pham, T. B. H. Phan, D. L. Tran and X. P. Nguyen, *Adv. Nat. Sci.: Nanosci. Nanotechnol.*, 2012, **3**, 015006.
- 25 L. Tong, D. Liu, J. Shi, X. Yang and H. Yang, *J. Mater. Sci.*, 2012, **47**, 132.
- 26 H. Peng, G. Liu, X. Dong, J. Wang, J. Xu and W. Yu, *J. Alloys Compd.*, 2011, **509**, 6930.
- 27 W. Wang, M. Zou and K. Chen, *Chem. Commun.*, 2010, **46**, 5100.
- 28 K. Ariga, T. Mori and J. P. Hill, *Adv. Mater.*, 2012, **24**, 158.
- 29 K. Ariga, A. Vinu, Y. Yamauchi, Q. Ji and J. P. Hill, *Bull. Chem. Soc. Jpn.*, 2012, **85**, 1.
- 30 K. K. Haldar, T. Sen, S. Mandal and A. Patra, *ChemPhysChem*, 2012, **13**, 3989.

- 31 P. Drake, H.-J. Cho, P.-S. Shih, C.-H. Kao, K.-F. Lee, C.-H. Kuo, X.-Z. Lin and Y.-J. Lin, *J. Mater. Chem.*, 2007, **17**, 4914.
- 32 T. Mossman, *J. Immunol. Methods*, 1983, **65**, 55.
- 33 S. Ishihara, N. Iyi, Y. Tsujimoto, S. Tominaka, Y. Matsushita, V. Krishnan, M. Akada, J. Labuta, K. Deguchi, S. Ohki, M. Tansho, T. Shimizu, Q. Ji, Y. Yamauchi, J. Hill, H. Abe and K. Ariga, *Chem. Commun.*, 2013, **49**, 3631.
- 34 A. Kar, S. Kundu and A. Patra, *J. Phys. Chem. C*, 2011, **115**, 118.
- 35 S. Dutta, S. Som and S. Sharma, *Dalton Trans.*, 2013, **42**, 9654.
- 36 V. S. Marques, L. S. Cavalcante, J. C. Sczancoski, A. F. P. Alcântara, M. O. Orlandi, E. Moraes, E. Longo, J. A. Varela, M. S. Li and M. R. M. C. Santos, *Cryst. Growth Des.*, 2010, **10**, 4752.
- 37 L. S. Cavalcante, V. M. Longo, J. C. Sczancoski, M. A. P. Almeida, A. A. Batista, J. A. Varela, M. O. Orlandi, E. Longo and M. S. Li, *CrystEngComm*, 2012, **14**, 853.
- 38 E. Sarantopoulou, C. Raptis, S. Ves, D. Christofilos and G. A. Kourouklis, *J. Phys.: Condens. Matter*, 2002, **14**, 8925.
- 39 A. K. Parchur, R. S. Ningthoujam, S. B. Rai, G. S. Okram, R. A. Singh, M. Tyagi, S. C. Gadkari, R. Tewari and R. K. Vatsa, *Dalton Trans.*, 2011, **40**, 7595.
- 40 N. K. Sahu, R. S. Ningthoujam and D. Bahadur, *J. Appl. Phys.*, 2012, **112**, 014306.
- 41 A. K. Parchur and R. S. Ningthoujam, *RSC Adv.*, 2012, **2**, 10859.
- 42 A. Xie, X. Yuan, S. Hail, J. Wang, F. Wang and L. Li, *J. Phys. D: Appl. Phys.*, 2009, **42**, 105107.
- 43 H. Wu, Y. Hu, W. Zhang, F. Kang, N. Li and G. Ju, *J. Sol-Gel Sci. Technol.*, 2012, **62**, 227.
- 44 R. S. Ningthoujam, L. Robindro Singh, V. Sudarsan and S. D. Singh, *J. Alloys Compd.*, 2009, **484**, 782.
- 45 S. Gago, M. Pillinger, R. A. Ferreira, L. D. Carlos, T. M. Santos and I. S. Gonçalves, *Chem. Mater.*, 2005, **17**, 5803.
- 46 A. I. Prasad, A. K. Parchur, R. R. Juluri, R. S. Ningthoujam and R. K. Vatsa, *Dalton Trans.*, 2013, **42**, 4885.
- 47 T. Förster, *Ann. Phys.*, 1948, **437**, 55.
- 48 D. L. Dexter, *J. Chem. Phys.*, 1953, **21**, 836.
- 49 N. V. Jadhav, A. I. Prasad, A. Kumar, R. Mishra, S. Dhara, K. R. Babu, C. L. Prajapat, N. L. Misra, R. S. Ningthoujam, B. N. Pandey and R. K. Vatsa, *Colloids Surf., B*, 2013, **108**, 158.
- 50 M. Geiser, B. Rothen-Rutishauser, N. Kapp, S. Schurch, W. Kreyling, H. Schulz, M. Semmler, V. I. Hof, J. Heyder and P. Gehr, *Environ. Health Perspect.*, 2005, **113**, 1555.
- 51 H. Yang, C. Liu, D. Yang, H. Zhang and Z. Xi, *J. Appl. Toxicol.*, 2009, **29**, 69.
- 52 T. Andelman, S. Gordonov, G. Busto, P. V. Moghe and R. E. Riman, *Nanoscale Res. Lett.*, 2009, **5**, 263.
- 53 E. Engelhaupt, L. Thrall, B. Booth and R. Chatterjee, *Environ. Sci. Technol.*, 2007, **41**, 3788.